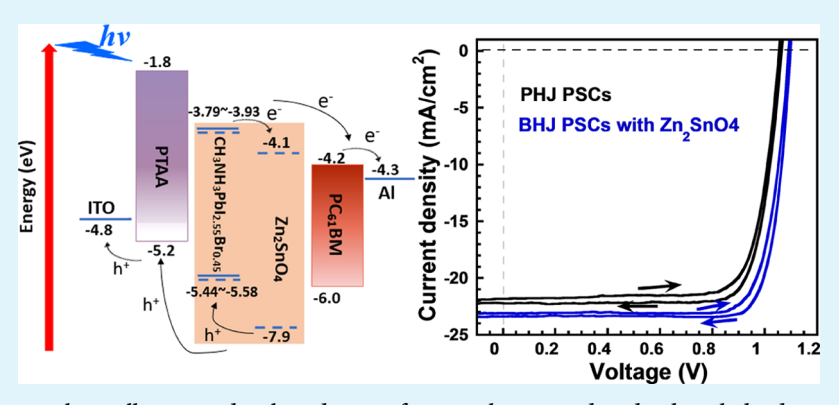


Bulk Heterojunction Perovskite Solar Cells Incorporated with Zn₂SnO₄ Nanoparticles as the Electron Acceptors

Wenzhan Xu, Luyao Zheng, Tao Zhu, Lei Liu, and Xiong Gong*

Department of Polymer Engineering, College of Polymer Science and Polymer Engineering, The University of Akron, Akron, Ohio 44325, United States

Supporting Information



ABSTRACT: Perovskite solar cells were developed very fast in the past decade, but hybrid perovskite materials with unbalanced charge carrier diffusion lengths were not fully addressed by either conventional or planar heterojunction device structures. In this study, high-performance perovskite solar cells with bulk heterojunction device structures where CH₃NH₃PbI_{2.55}Br_{0.45} is blended with an n-type high-electron-mobility Zn₂SnO₄ nanoparticle as the photoactive layer are reported. Systematic studies indicate that the CH₃NH₃PbI_{2.55}Br_{0.45}:Zn₂SnO₄ bulk heterojunction thin film possesses enhanced and balanced charge carrier mobilities, superior film morphology with enlarged crystal sizes, and suppressed trap density. Photoluminescence and time-resolved photoluminescence studies further demonstrate that there is an efficient photoinduced charge carrier transfer between CH₃NH₃PbI_{2.55}Br_{0.45} and Zn₂SnO₄ nanoparticles. Thus, bulk heterojunction perovskite solar cells by the CH₃NH₃PbI_{2.55}Br_{0.45}:Zn₂SnO₄ thin film exhibit over 21.07% power conversion efficiency, which is more than 12% enhancement as compared to that (18.74%) observed from planar heterojunction perovskite solar cells by the pristine CH₃NH₃PbI_{2.55}Br_{0.45} thin film. Moreover, bulk heterojunction perovskite solar cells possess significantly suppressed photocurrent hysteresis, dramatically enhanced device stability, and reproducibility. All these results demonstrate that high-performance perovskite solar cells can be realized through bulk heterojunction device structures.

KEYWORDS: perovskite solar cells, bulk heterojunction device structure, Zn₂SnO₄ nanoparticles, electron acceptors, device performance

■ INTRODUCTION

In the last decade, there has been great attention to perovskite solar cells (PSCs) in both the academic and industrial sectors. Over 25% power conversion efficiency (PCE) has been reported from PSCs with conventional device structures where a mesoporous titanium dioxide (ms-TiO₂) scaffold layer serves as the electron extraction layer (EEL) for effectively transporting separated electrons from the hybrid perovskite layer to the indium tin oxide (ITO) cathode. However, the ms-TiO₂ EEL was required to be sintered at high temperature (over 500 °C), which certainly restricted PSCs to be cost-effectively manufactured on the flexible substrates. Alternatively, PSCs with planar heterojunction (PHJ) device structures, which potentially can be processed on the flexible substrates, were developed to circumvent the problems from PSCs with conventional device structures. In PHJ PSCs,

low-temperature solution-processed poly(3,4-ethylenedioxythiophene):polystyrene sulfonate (PEDOT:PSS) has been typically employed as the hole extraction layer (HEL), and a solution-processed fullerene derivative typically serves as the EEL. $^{9-13}$ PSCs with above two different device structures have been rapidly developed; however, the diffusion length of the hole that is greater than that of the electron $(L_{\rm eff,\ h}^+/L_{\rm eff,\ e}^->1)$ of hybrid perovskite has not been fully addressed so far. $^{1-5,12-15}$

In order to address such unbalanced electron and hole diffusion lengths within hybrid perovskite materials, we first reported bulk heterojunction (BHJ) PSCs where methyl-

Received: July 14, 2019 Accepted: August 21, 2019 Published: August 21, 2019



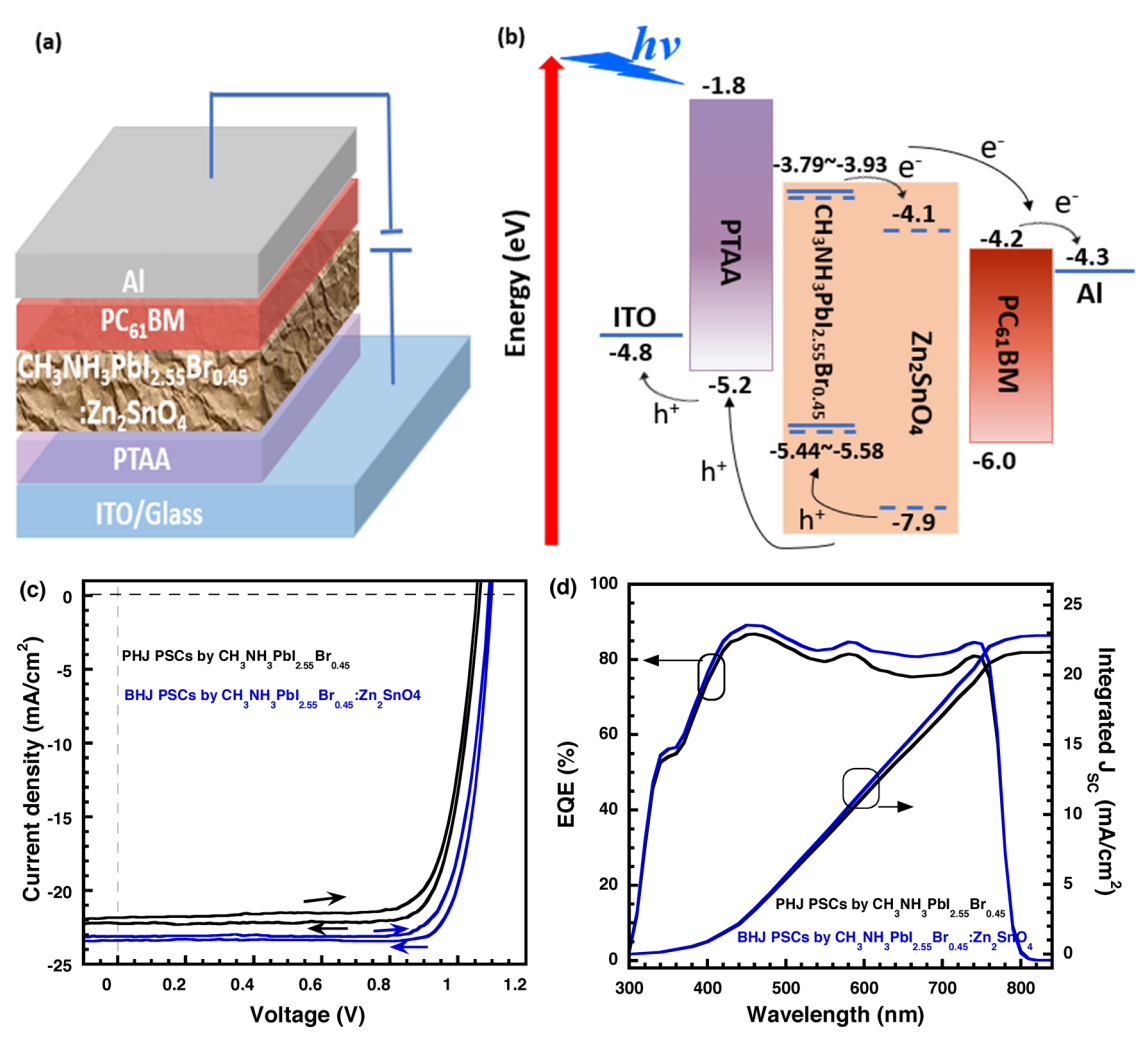


Figure 1. (a) Device structure of BHJ PSCs, (b) the work functions of ITO and Al electrodes and the LUMO and HOMO energy levels of PTAA, $CH_3NH_3PbI_{2.55}Br_{0.45}$, Zn_2SnO_4 NPs, and $PC_{61}BM$, (c) the J-V characteristics, and (d) EQE spectra and integrated J_{SC} of PHJ PSCs and BHJ PSCs.

ammonium lead halides were blended with fullerene derivatives for balancing charge transporting properties. 16,17 Further studies found that BHJ composites not only facilitate charge carrier extraction efficiency but also optimize film morphology of the photoactive layer, resulting in boosted PCEs. 16-23 However, fullerene derivatives were hardly homogeneously mixed with hybrid perovskite materials due to their poor solubility in the solvent used for dissolving precursors for generating perovskite thin films. 16-23 Moreover, fullerene derivatives possess poor electron mobilities.²⁴ All these shortcomings restricted further boosted device performances of PSCs. $^{16-24}$ In this study, we report high-performance BHJ PSCs where CH3NH3PbI2.55Br0.45 is blended with the Zn₂SnO₄ nanoparticle (NP) as the photoactive layer. The ntype semiconductor Zn₂SnO₄ NP is selected as the electron acceptor since it possesses high electron mobility and it has been popular as the EEL in both organic photovoltaics and 5,26 Most importantly, Zn₂SnO₄ NPs have excellent solubility in anhydrous N,N-dimethylformamide (DMF), which is a solvent typically used for dissolving PbI₂, a precursor for forming hybrid perovskite. As compared with the pristine $CH_3NH_3PbI_{2.55}Br_{0.45}$ thin film, the CH₃NH₃PbI_{2.55}Br_{0.45}:Zn₂SnO₄ BHJ composite thin film possesses enhanced and balanced charge carrier mobilities,

superior film quality with enlarged crystal sizes, and suppressed trap density. Photoluminescence and time-resolved photoluminescence studies indicate that there is an efficient photoinduced charge carrier transfer between CH₃NH₃PbI_{2.55}Br_{0.45} and Zn₂SnO₄ NPs. As a result, BHJ PSCs by the CH₃NH₃PbI_{2.55}Br_{0.45}:Zn₂SnO₄ thin film exhibit enhanced PCEs, dramatically reduced photocurrent hysteresis, improved device stability, and high reproducibility as compared to PHJ PSCs by the pristine CH₃NH₃PbI_{2.55}Br_{0.45} thin film.

■ RESULTS AND DISCUSSION

The preparation and characterization of Zn₂SnO₄ NPs are described in the Experimental Section and detailed in Section S1. The BHJ PSC device structure of ITO/PTAA/CH₃NH₃PbI_{2.55}Br_{0.45}:Zn₂SnO₄/PC₆₁BM/Al, where ITO is indium tin oxide and serves as the anode, PTAA is poly[bis(4-phenyl)(2,4,6-trimethyl phenyl)amine] and serves as the HEL, PC₆₁BM is [6,6]-phenyl C₆₁-butyric acid methyl ester and serves as the EEL, and Al is aluminum and serves as the cathode, is shown in Figure 1a. The highest occupied molecular orbital (HOMO) and the lowest unoccupied molecular orbital (LUMO) energy levels of PTAA, CH₃NH₃PbI_{2.55}Br_{0.45}, Zn₂SnO₄ NPs, and PC₆₁BM and the

Table 1. Device Performance Parameters of PSCs^a

$CH_3NH_3PbI_{2.55}Br_{0.45}:x\%\ Zn_2SnO_4$	$V_{\rm OC}$ (V)	$J_{\rm SC}~({\rm mA~cm^{-2}})$	FF (%)	PCE (%)	$R_{\rm S}~(\Omega~{ m cm}^{-2})$	$R_{\rm SH}~(\Omega~{ m cm}^{-2})$
0.0	1.06 (1.03)	22.23 (21.02)	79 (78)	18.74 (17.38)	15.34	734.25
5	1.08 (1.04)	22.96 (22.05)	80 (79)	19.93 (18.82)	10.56	921.98
10	1.10 (1.05)	23.34 (22.76)	82 (81)	21.07 (20.25)	8.74	1363.28
15	1.03 (1.05)	22.03 (20.75)	75 (73)	17.32 (15.74)	21.58	629.01
^a Performance metrics in parentheses are average values.						

(a) $CH_3NH_3Pbl_{2.55}Br_{0.45}:Zn_2SnO_4$ CH₃NH₃Pbl_{2 55}Br_{0 45} 500 nm 500 nm (d) (c) CH₃NH₃Pbl_{2,55}Br_{0,45}:Zn₂SnO CH₃NH₃Pbl_{2.55}Br_{0.45} CH₂NH₂Pbl_{2.55}Br_{0.45} PL Intensity (a.u.) CH₃NH₃Pbl₂₅₅Br₀₄₅:Zn₂SnO₄ PL Intensity 0.6 0.4 0.2 10 650 700 Time (ns)

Figure 2. Top-view SEM images of (a) pristine CH₃NH₃PbI_{2.55}Br_{0.45} thin film and (b) the CH₃NH₃PbI_{2.55}Br_{0.45};Zn₂SnO₄ BHJ composite thin film on the top of PTAA/ITO, (c) the photoluminescence (PL) spectra, and (d) time-resolved PL spectra of pristine CH3NH3PbI2.55Br0.45 thin film and the CH₃NH₃PbI_{2.55}Br_{0.45}:Zn₂SnO₄ BHJ composite thin film.

work functions of ITO and Al are presented in Figure 1b. Based on the band alignment shown in Figure 1b, both LUMO and HOMO energy offsets between CH3NH3PbI2.55Br0.45 and Zn₂SnO₄ NPs are larger than 0.2 eV,²⁷ which can ensure that the photoinduced charge transfer process takes place between CH₃NH₃PbI_{2.55}Br_{0.45} and Zn₂SnO₄ NPs, resulting in enhanced photocurrent and, consequently, boosted PCEs.

Wavelength (nm)

The current density versus voltage (J-V) characteristics of PSCs under different scan directions are shown in Figure 1c. The device performance parameters are summarized in Table 1. Under a scan rate of 0.6 V s⁻¹, PHJ PSCs by the pristine CH3NH3PbI2.55Br0.45 thin film exhibit a short-circuit current (J_{SC}) of 22.23 mA cm⁻², an open-circuit voltage (V_{OC}) of 1.06 V, and a fill factor (FF) of 79%, with a corresponding PCE of 18.74%. These device performance parameters well agree with the reported values. $^{1-6}$ BHJ PSCs by the $CH_3NH_3PbI_{2.55}Br_{0.45}$: Zn_2SnO_4 composite thin film, where the concentration of Zn₂SnO₄ NPs is ~5% (by weight) in the BHJ composite, exhibit a J_{SC} of 22.96 mA cm⁻², a V_{OC} of 1.08 V, and an FF of 80%, with a corresponding PCE of

19.93%. BHJ PSCs by the CH₃NH₃PbI_{2.55}Br_{0.45}:Zn₂SnO₄ composite thin film, where the concentration of Zn₂SnO₄ NPs is \sim 10% (by weight) in the BHJ composite, show a $J_{\rm SC}$ of 23.34 mA cm⁻², a V_{OC} of 1.10 V, and an FF of 82%, with a resultant PCE of 21.07%. These results indicate an over 12% improvement in PCE as compared with that from PHJ PSCs by the pristine CH₃NH₃PbI_{2.55}Br_{0.45} thin film. However, as the concentration of Zn₂SnO₄ NPs is further increased to 15%, BHJ PSCs by the CH₃NH₃PbI_{2.55}Br_{0.45}:Zn₂SnO₄ composite thin film exhibit a decreased PCE (17.32%). The device performances of BHJ PSCs correlated with the ratios and particle sizes of Zn₂SnO₄ NPs in the CH₃NH₃PbI_{2.55}Br_{0.45}:Zn₂SnO₄ BHJ composite thin films are described in Section S2.

The external quantum efficiency (EQE) spectra of PSCs are shown in Figure 1d. As compared with PHJ PSCs, an enhancement in the wavelength ranging from 380 to 760 nm can be found in the EQE spectrum of BHJ PSCs. These results indicate that BHJ PSCs by the CH3NH3PbI2.55Br0.45:Zn2SnO4 composite thin film generate more photocurrents than PHJ

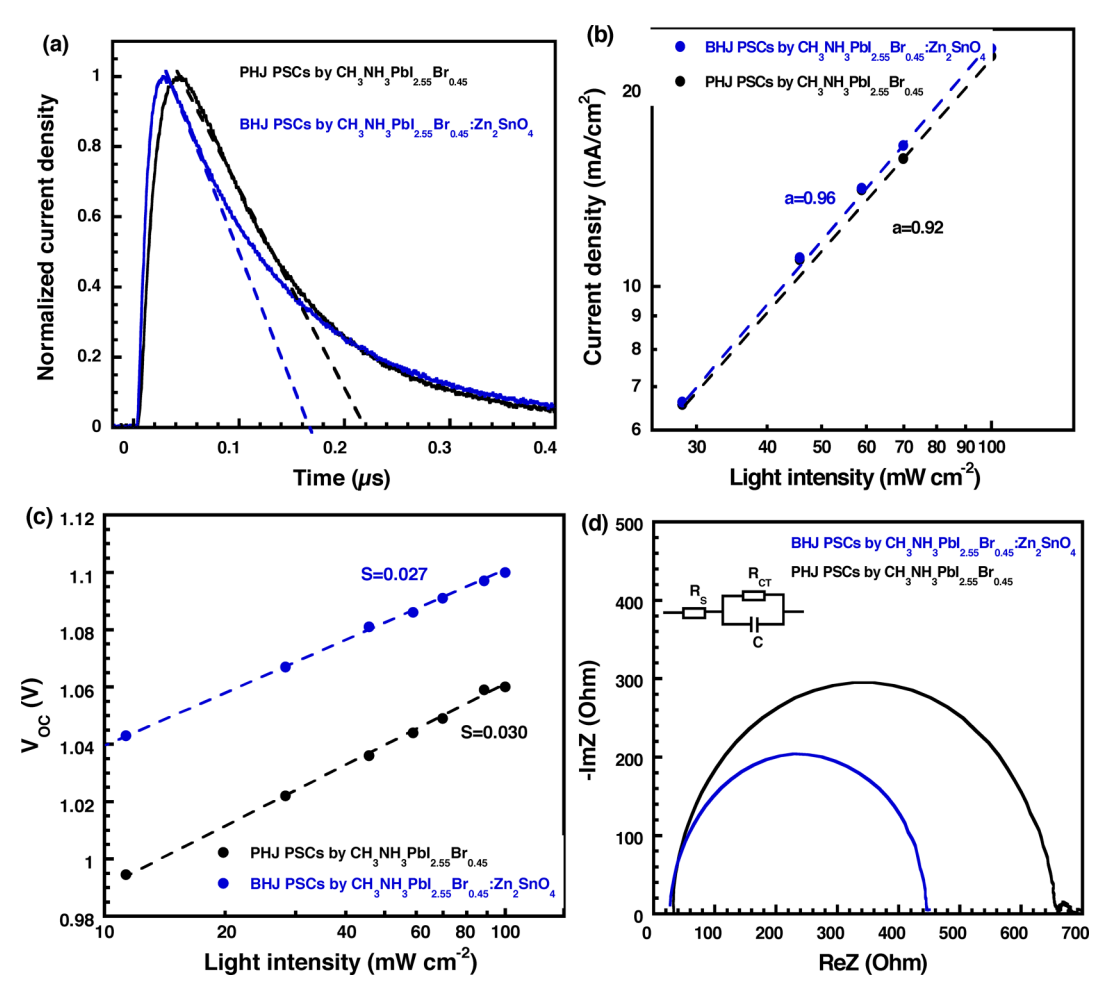


Figure 3. (a) Normalized photocurrent decay of PSCs under the short-circuit condition, the light-intensity dependence of (b) the steady-state short-circuit current (the dotted lines represent fits to the expression $I_{\rm SC} \propto I^{\alpha}$) and (c) the steady-state open circuit voltage (the dotted lines represent fits to the expression $V_{\rm OC} = SIn(I/I_0)$) of PSCs, and (d) the Nyquist plots of PSCs measured in the dark and under an applied voltage close to the open-circuit voltage of PSCs.

PSCs by the pristine $CH_3NH_3PbI_{2.55}Br_{0.45}$ thin film. By integrating the EQE spectra over wavelength, BHJ PSCs and PHJ PSCs present estimated J_{SC} values of 22.93 and 21.72 mA cm⁻², respectively. These estimated J_{SC} values well match with J_{SC} values obtained by the J-V characteristics (Figure 1c).

In order to investigate the enhancement on device performances of PSCs, the film morphologies and crystallinities of photoactive layers are first studied. The top-view scanning electron microscope (SEM) images of the pristine $\begin{array}{c} C~H_{3}~N~H_{3}~P~b~I_{2..5~5}~B~r_{0..4~5} & t~h~i~n~~fi~l~m~~a~n~d~~t~h~e~\\ CH_{3}NH_{3}PbI_{2.55}Br_{0.45}:Zn_{2}SnO_{4}~BHJ~composite~thin~film~~are \end{array}$ displayed in Figure 2a,b. Lots of voids with large grain boundaries are observed from the pristine $CH_3NH_3PbI_{2.55}Br_{0.45}$ thin film, whereas the CH₃NH₃PbI_{2.55}Br_{0.45}:Zn₂SnO₄ BHJ composite thin film exhibits much less pinholes with dramatically reduced grain boundaries and relatively uniform crystals. The average crystal size of $CH_3NH_3PbI_{2.55}Br_{0.45}$ in the CH₃NH₃PbI_{2.55}Br_{0.45}:Zn₂SnO₄ BHJ composite thin film is \sim 400 nm, which is significantly larger than that (\sim 150 nm) observed from the pristine CH₃NH₃PbI_{2.55}Br_{0.45} thin film. To further verify film morphological differences in the pristine $CH_3NH_3PbI_{2.55}Br_{0.45}$ thin film and the $CH_3NH_3PbI_{2.55}Br_{0.45}$: Zn_2SnO_4 BHJ composite thin film, the film morphologies of precursor layers PbI₂ and PbI₂:Zn₂SnO₄

are studied (Section S3). Two-dimensional (2D) grazingincidence wide-angle X-ray scattering (GIWAXS) patterns indicate that both PbI2 and PbI2:Zn2SnO4 thin films exhibit typical scattering peaks for PbI2 crystals, but the emerged rings, corresponding to Zn₂SnO₄ NPs, are observed from the PbI2:Zn2SnO4 thin film. Moreover, network-like lavered crystals ranging from tens to several hundreds of nanometers in size with many voids are observed from the PbI2 thin film, whereas the PbI₂:Zn₂SnO₄ thin film has a much more uniform and dense surface (Figure S4). All these results imply that the formation of the CH3NH3PbI2.55Br0.45 crystals in the $CH_3NH_3PbI_{2.55}Br_{0.45}:Zn_2SnO_4$ BHJ composite thin film probably takes a longer time than that of the pristine CH₃NH₃PbI_{2.55}Br_{0.45} thin film. Consequently, the CH₃NH₃PbI_{2.55}Br_{0.45}:Zn₂SnO₄ thin film forms high-quality film morphology with large crystal size but few pinholes. 28,29 Furthermore, 1D GIWAXS patterns (Figure S6) indicate that there is a new peak located at ~ 3.5 Å⁻¹ in the CH₃NH₃PbI_{2.55}Br_{0.45}:Zn₂SnO₄ BHJ composite thin film. Such a new peak is probably attributed to Zn₂SnO₄ NPs with a crystal structure rather than a cubic crystal structure. 25,26,30,31 In addition, substantially increased scattering intensities and enlarged full widths at half-maximum of the (110), (220), (310), and (224) planes observed from the CH₃NH₃PbI_{2.55}Br_{0.45}:Zn₂SnO₄ BHJ composite thin film further confirm that the $CH_3NH_3PbI_{2.55}Br_{0.45}$: Zn_2SnO_4 BHJ composite thin film indeed forms superior crystallinity, superior film morphology, and larger crystals. All these features are favorable for the $CH_3NH_3PbI_{2.55}Br_{0.45}$: Zn_2SnO_4 BHJ composite thin film to efficiently transport charge carriers, resulting in high J_{SC} for BHJ PSCs.

Figure 2c presents the steady-state photoluminescence (PL) spectra of pristine CH₃NH₃PbI_{2.55}Br_{0.45} and the CH₃NH₃PbI_{2,55}Br_{0,45}:Zn₂SnO₄ BHJ composite thin films. The emission spectrum of the pristine CH₃NH₃PbI_{2.55}Br_{0.45} thin film shows a peak at 770 nm, which corresponds to the nanocrystalline perovskite particles. 1-6 The CH₃NH₃PbI_{2.55}Br_{0.45}:Zn₂SnO₄ BHJ composite thin film possesses an identical emission spectral shape and location to the pristine CH₃NH₃PbI_{2.55}Br_{0.45} thin film but with a dramatically quenched PL intensity. In order to investigate the striking PL quenching effect, absorption spectra of pristine $CH_3NH_3PbI_{2.55}Br_{0.45}$ and the $CH_3NH_3PbI_{2.55}Br_{0.45}$: Zn_2SnO_4 BHJ composite thin films are recorded (Section S4). Pristine $CH_{3}NH_{3}PbI_{2.55}Br_{0.45} \ \ and \ \ the \ \ CH_{3}NH_{3}PbI_{2.55}Br_{0.45}{:}Zn_{2}SnO_{4}$ BHJ composite thin films exhibit similar absorption spectral shapes, but the CH₃NH₃PbI_{2.55}Br_{0.45}:Zn₂SnO₄ BHJ composite thin film possesses a slight red-shift at the cutoff wavelength, which is ascribed to the denser crystal order of CH₃NH₃PbI_{2.55}Br_{0.45} induced by Zn₂SnO₄ NPs.^{28,29} The dramatically quenched PL intensity observed from the CH₃NH₃PbI_{2.55}Br_{0.45}:Zn₂SnO₄ BHJ composite thin film indicates that there is an efficient photoinduced charge transfer process between CH₃NH₃PbI_{2.55}Br_{0.45} and Zn₂SnO₄ NPs. ¹⁶⁻²¹ In the issue, enhanced J_{SC} is expected from BHJ PSCs by the CH₃NH₃PbI_{2.55}Br_{0.45}:Zn₂SnO₄ BHJ composite thin film.

Figure 2d displays the time-resolved PL spectra of pristine $CH_3NH_3PbI_{2.55}Br_{0.45}$ and $CH_3NH_3PbI_{2.55}Br_{0.45}:Zn_2SnO_4$ BHJ composite thin films. The $CH_3NH_3PbI_{2.55}Br_{0.45}:Zn_2SnO_4$ BHJ composite thin film possesses a longer charge carrier lifetime than the pristine $CH_3NH_3PbI_{2.55}Br_{0.45}$ thin film, indicating the elongated charge carrier diffusion length of the $CH_3NH_3PbI_{2.55}Br_{0.45}:Zn_2SnO_4$ BHJ composite thin film. Thus, increased J_{SC} values, which ultimately lead to enhanced PCEs from BHJ PSCs, are observed.

Figure 3a shows the normalized transient photocurrent (TPC) spectra of PSCs where the measurement is conducted (Section S5). The charge extraction time, by extrapolating the linear region to zero, 5,33 for BHJ PSCs by the CH₃NH₃PbI_{2.55}Br_{0.45}:Zn₂SnO₄ BHJ composite thin film is estimated to be \sim 175 ns, which is faster than that (\sim 205 ns) for PHJ PSCs by the pristine CH₃NH₃PbI_{2.55}Br_{0.45} thin film, indicating that BHJ PSCs possess a restricted charge carrier recombination process than PHJ PSCs.34-36 Moreover, both PSCs show similar charge carrier sweep-out processes, but they are dramatically different after the process took place ~50 ns (Figure S9). About over 12% of charge carrier density, by integration of the TPC density over time, 36 is profitably swept out in BHJ PSCs compared to PHJ PSCs. These results indicate that BHJ PSCs exhibit an enhanced J_{SC} . This observation is consistent very well with the J-V characteristics (Figure 1c).

To further reveal underlying physics of boosted J_{SC} , both charge carrier traps and mobilities of pristine CH₃NH₃PbI_{2.55}Br_{0.45} and CH₃NH₃PbI_{2.55}Br_{0.45}:Zn₂SnO₄ BHJ composite thin films are investigated. According to the Mott–Gurney law, ^{37,38} both charge carrier trap densities and mobilities are obtained from the J-V characteristics observed

from either the hole-only or the electron-only device (Section S6). The hole-trap and electron-trap densities of the pristine $CH_3NH_3PbI_{2.55}Br_{0.45}$ thin film are estimated to be 9.19×10^{15} and 4.98×10^{15} cm⁻³, respectively. The estimated hole-trap density of the CH₃NH₃PbI_{2.55}Br_{0.45}:Zn₂SnO₄ BHJ composite thin film is 2.44×10^{15} cm⁻³, which is 4 times smaller than that of the pristine CH₃NH₃PbI_{2.55}Br_{0.45} thin film, and the estimated electron-trap density of the CH₃NH₃PbI_{2.55}Br_{0.45}:Zn₂SnO₄ BHJ composite thin film is 2.36×10^{15} cm⁻³, which is approximatively twice smaller than that of the pristine CH₃NH₃PbI_{2.55}Br_{0.45} thin film. The hole and electron mobilities of the pristine CH₃NH₃PbI_{2.55}Br_{0.45} thin film are estimated to be 1.12×10^{-2} and 4.98×10^{-3} cm² V⁻¹ s⁻¹, respectively. The hole and electron mobilities of the CH₃NH₃PbI_{2.55}Br_{0.45}:Zn₂SnO₄ BHJ composite thin film are estimated as 3.26×10^{-2} and 6.94×10^{-2} cm 2 V $^{-1}$ s $^{-1}$, respectively. The hole mobility of the $CH_3NH_3PbI_{2.55}Br_{0.45}$: Zn_2SnO_4 BHJ composite thin film is about 3 times larger than that of the pristine CH₃NH₃PbI_{2.55}Br_{0.45} thin film, and the electron mobility of the CH₃NH₃PbI_{2.55}Br_{0.45}:Zn₂SnO₄ BHJ composite thin film is approximatively 14 times larger than that of the pristine CH₃NH₃PbI_{2.55}Br_{0.45} thin film. The synchronously enhanced electron and hole mobilities for the CH₃NH₃PbI_{2.55}Br_{0.45}:Zn₂SnO₄ BHJ composite thin films are due to the reduced electron-trap and hole-trap densities, less crystal imperfections, and reduced structural defects. From this aspect, boosted J_{SC} is found from BHJ PSCs by the CH₃NH₃PbI_{2.55}Br_{0.45}:Zn₂SnO₄ BHJ composite thin film.

Steady-state light-intensity dependence on both $V_{\rm OC}$ and $J_{\rm SC}$ is further studied to investigate charge carrier recombination in PSCs. Figure 3b,c presents the light-intensity-dependent J_{SC} and $V_{\rm OC}$ for both PSCs. A coefficient of α = 0.96, according to the power law fit $J_{SC} \propto I^{\alpha}$ (where I is the light intensity), ^{39,40} is observed from BHJ PSCs, whereas a coefficient of $\alpha = 0.92$ is observed from PHJ PSCs. The higher α value reveals that BHJ PSCs exhibit suppressed charge carrier recombination.³⁹ Furthermore, a slope of S = 0.027 (1.05kT/q), which is based on $V_{\rm OC} = SIn(I/I_0)$ (where k is Boltzmann's constant, T is the temperature, and q is the elementary charge), 39,40 is observed from BHJ PSCs, whereas a slope of S = 0.030(1.16kT/q) is observed from PHJ PSCs. The smaller the slope S, the lower the possibility of trap-assisted charge carrier recombination to take place. ^{39–41} Thus, higher α and smaller Sobserved from BHJ PSCs indicate that charge carrier recombination is suppressed in BHJ PSCs. Therefore, BHJ PSCs by the $CH_3NH_3PbI_{2.55}Br_{0.45}$: Zn_2SnO_4 thin film exhibit boosted PECs.

Impedance spectroscopy is commonly used in solar cells to study the interfacial dynamics of charge carrier transport and charge carrier recombination because it is capable of distinguishing dynamic processes inside the operating devices according to their response to the externally applied alternating current signal. Figure 3d displays impedance spectra for PSCs measured in the dark under a bias close to $V_{\rm OC}$ of PSCs. A simplified circuit model is presented in Figure 3d, which is composed of the sheet resistance $(R_{\rm S})$ of the conductive electrodes and the charge transfer resistance $(R_{\rm CT})$ affected by film morphologies and crystal structures of active layers. $R_{\rm S}$ is assumed to be the same because both PSCs possess the same electrodes. The $R_{\rm CT}$ value of PHJ PSCs is estimated to be 665 Ω , whereas the $R_{\rm CT}$ value of BHJ PSCs is estimated to be 448 Ω . The smaller $R_{\rm CT}$ observed from BHJ PSCs originates from

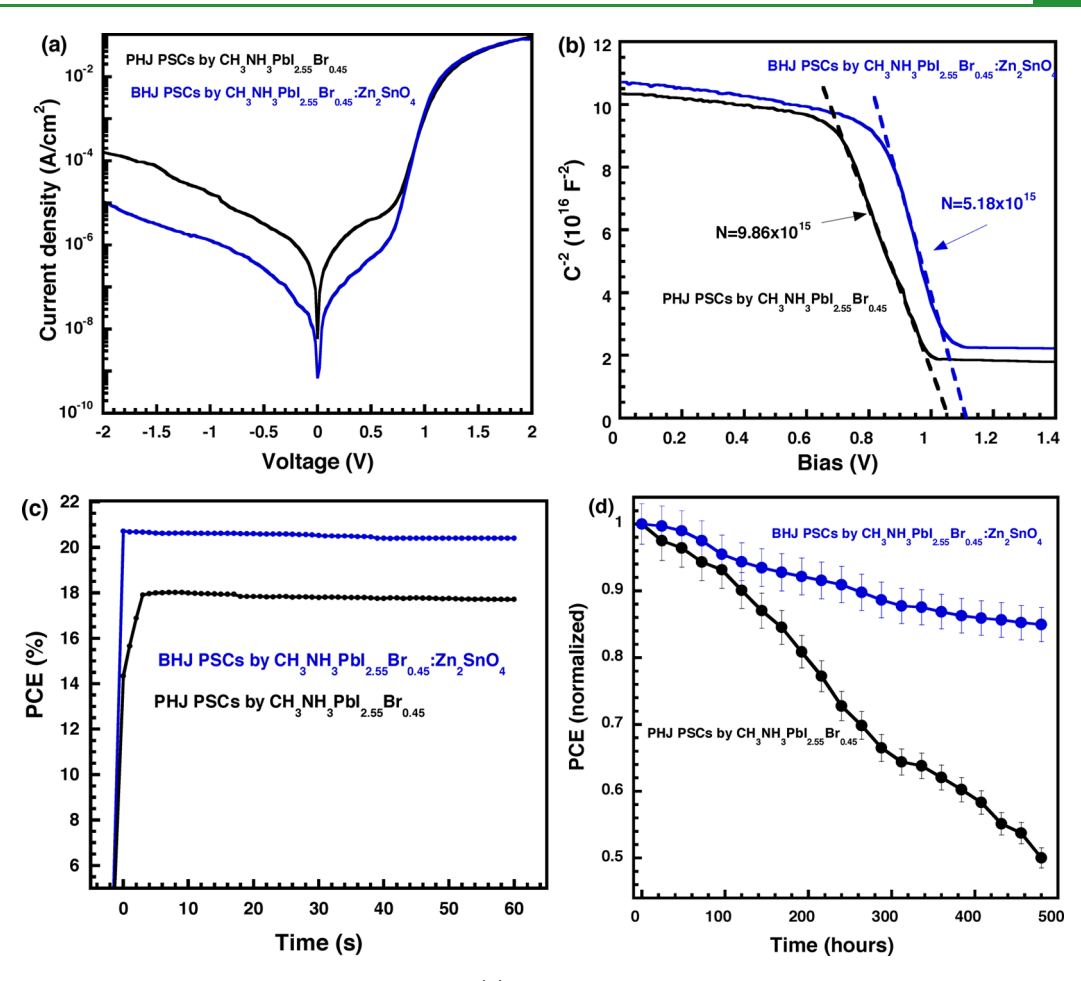


Figure 4. (a) *J–V* characteristics of PSCs measured in the dark, (b) the Mott–Schottky analysis for the interfacial trap -density and the built-in potential of PSCs, (c) the steady-state photocurrent output of PSCs at the maximum power point, and (d) the shelf stability of PSCs.

the high-quality thin film with superior surface coverage and enhanced charge carrier mobility of the $CH_3NH_3PbI_{2.55}Br_{0.45}$: Zn_2SnO_4 thin film. Thus, as expected, high J_{SC} and FF with corresponding boosted PCE are observed from BHJ PSCs by the $CH_3NH_3PbI_{2.55}Br_{0.45}$: Zn_2SnO_4 thin film.

The J-V characteristics of PSCs measured in the dark are shown in Figure 4a. Under reverse biases, the dark current densities of PHJ PSCs are approximatively 10 times larger than those from BHJ PSCs, which illustrates that charge carrier recombination is restricted in BHJ PSCs. Moreover, according to $V_{\rm OC} \approx \frac{nkT}{q} \ln \frac{J_{\rm SC}}{J_0}$, where J_0 is the reverse dark current density, q is the electron charge, n is the diode ideality factor, k is Boltzmann's constant, and T is the temperature, a low value of J_0 indicates a large value of $V_{\rm OC}$ for solar cells. Thus, BHJ PSCs exhibit larger $V_{\rm OC}$ than PHJ PSCs. This observation is in good match with the J-V characteristics.

The classic Mott–Schottky (M–S) relation, based on the capacitance–voltage (C-V) characteristics, is further employed to estimate the built-in potential $(V_{\rm bi})$ and the interfacial charge density (N) of PSCs. The $V_{\rm bi}$ is the intercept on the bias axis of the linear fitting line and the N is obtained from the slope of the linear fitting line, respectively, ^{46,47} and the resultant curves are presented in Figure 4b. A $V_{\rm bi}$ of 1.12 V, which is larger than that $(1.06~{\rm V})$ for PHJ PSCs, is observed from BHJ PSCs. Thus, BHJ PSCs possess larger $V_{\rm OC}$ than PHJ PSCs. Moreover, the slope of the $C^{-2}-V$ characteristics for

PHJ PSCs is estimated to be -2.65×10^{17} , whereas the slope of the $C^{-2}-V$ characteristics for BHJ PSCs is estimated to be -3.38×10^{17} . A larger absolute value of the slope indicates that PSCs possess a smaller interfacial charge density. As a result, the charge carrier recombination is suppressed. Therefore, BHJ PSCs exhibit boosted $J_{\rm SC}$ compared to PHJ PSCs.

The photocurrent hysteresis is also primarily studied. The photocurrent hysteresis is quantitatively described by the hysteresis index HI = $\frac{\text{PCE}_{\text{reverse}} - \text{PCE}_{\text{forward}}}{\text{PCE}_{\text{reverse}}},^{49} \text{ where PCE}_{\text{reverse}} \text{ and }$

PCE_{forward} are PCEs of PSCs under either reverse or forward directions, respectively. Tables S1 and S2 summarize the HI values of PSCs. Under a scan rate of 0.6 V s⁻¹, PHJ PSCs by the pristine CH3NH3PbI2.55Br0.45 thin film exhibit an HI of 3.31, whereas BHJ PSCs by the CH₃NH₃PbI_{2.55}Br_{0.45}:Zn₂SnO₄ thin film, where the CH3NH3PbI2.55Br0.45:Zn2SnO4 thin films are incorporated with different ratios of Zn₂SnO₄ NPs, exhibit different HI values. The smallest HI value is observed from BHJ PSCs by the CH₃NH₃PbI_{2.55}Br_{0.45}:Zn₂SnO₄ thin film where the concentration of Zn₂SnO₄ NPs is 10% Zn₂SnO₄ NPs. Moreover, under a scan rate of 0.03 V s⁻¹, BHJ PSCs by the CH₃NH₃PbI_{2.55}Br_{0.45}:Zn₂SnO₄ thin film, where the concentration of Zn₂SnO₄ NPs is 10%, also possess smaller HI values than PHJ PSCs by the pristine CH₃NH₃PbI_{2.55}Br_{0.45} thin film. Thus, the photocurrent hysteresis is suppressed in BHJ PSCs. To further study the photocurrent hysteresis, the steady-state efficiency by operating the device at the maximum power voltage and allowing the photocurrent to be stabilized is

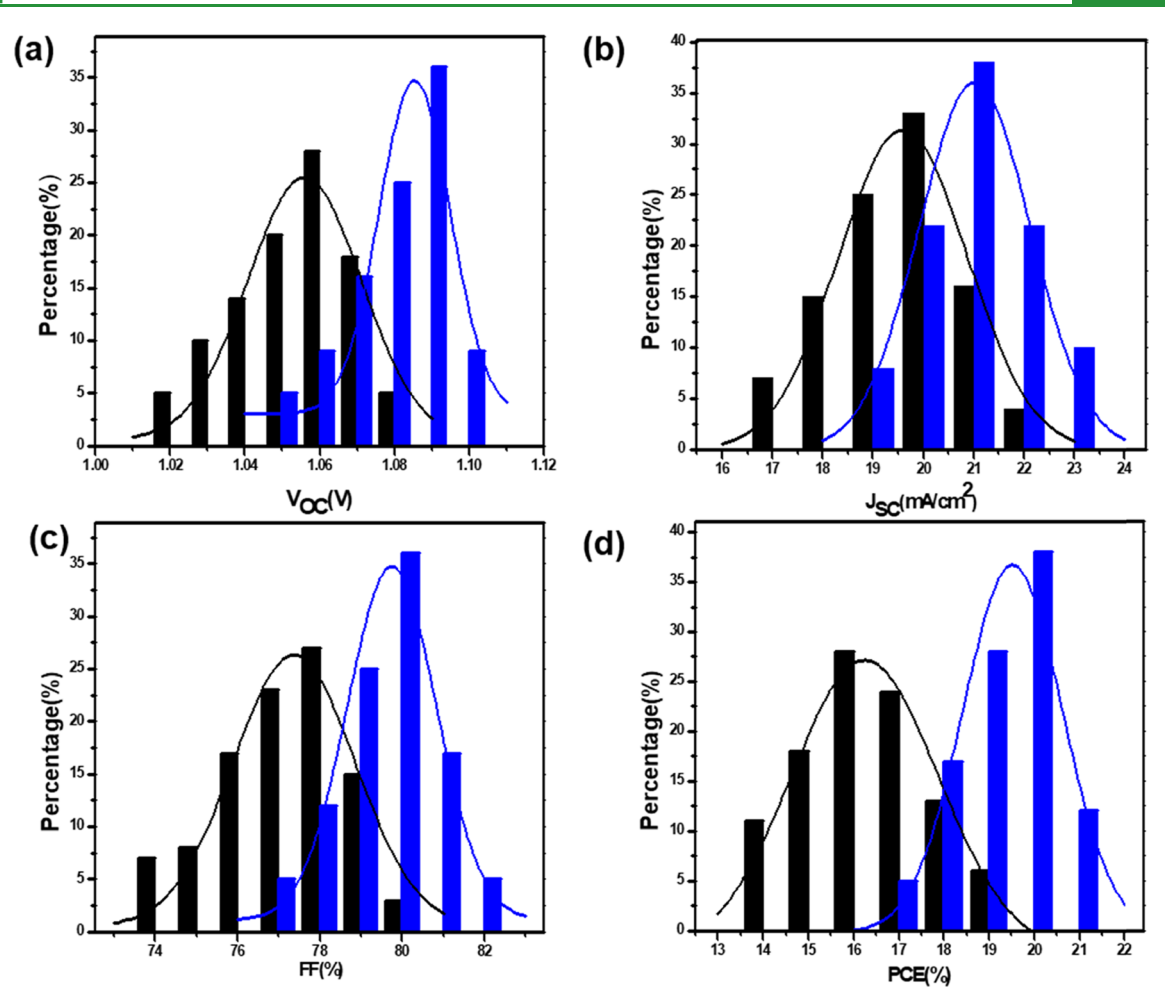


Figure 5. Histograms of device performance parameters for PSCs fabricated by either pristine CH₃NH₃PbI_{2.55}Br_{0.45}; thin film (black color) or the CH₃NH₃PbI_{2.55}Br_{0.45}; Zn₂SnO₄ thin film (blue color) with counted device numbers of n = 100 for each type (devices were measured under reverse scan with 0.6 V s⁻¹): (a) V_{OC} , (b) J_{SC} , (c) FF, and (d) PCE.

studied, and the results are displayed in Figure 4c. BHJ PSCs exhibit a PCE of 21.04% instantly, whereas PHJ PSCs exhibit a PCE of 18.70 over 15 s. These results demonstrate that BHJ PSCs possess suppressed photocurrent hysteresis. It was reported that photocurrent hysteresis is a multifactorial phenomenon that is influenced by the composition of the absorber, the trap density, the internal and external interfaces, and the crystal grains. As described above, the $CH_3NH_3PbI_{2.55}Br_{0.45}:Zn_2SnO_4$ thin film exhibits a less trap density, smooth surface, and dramatically minimized grain boundary, and thus, as expected, BHJ PSCs exhibit suppressed photocurrent hysteresis.

The stability of PSCs is one of the priority concerns for commercialization of PSCs. Figure 4d displays the shelf stability of PSCs where PSCs are unencapsulated but are stored in a glove box with an O₂ level of about 200 ppm. After 20 days, PCE of BHJ PSCs maintains 84.5% of its initial value, while PCE of PHJ PSCs drops to half of its initial value. These results indicate that BHJ PSCs possess superior stability compared to PHJ PSCs.

The reproducibility of PSCs is further studied. The statistical histograms of the photovoltaic parameters with Gaussian fitting for both PSCs from counted numbers of n=100 are shown in Figure 5. PHJ PSCs exhibit a severe deviation in $J_{\rm SC}$, $V_{\rm OC}$, FF, and PCE, compared to those observed from BHJ PSCs. Thus, the reproducibility of BHJ PSCs is significantly

higher than that of PHJ PSCs. The higher reproducibility of BHJ PSCs is ascribed to superior film quality and enlarged crystal sizes of the $\text{CH}_3\text{NH}_3\text{PbI}_{2.55}\text{Br}_{0.45}$ thin film owing to the presence of Zn_2SnO_4 NPs.

CONCLUSIONS

In summary, we reported high-performance bulk heterojunction (BHJ) perovskite solar cells (PSCs) where CH₃NH₃PbI_{2.55}Br_{0.45} was blended with high-electron-mobility Zn₂SnO₄ nanoparticle (NP) electron acceptors as the photoactive layers. It was found that the CH₃NH₃PbI_{2.55}Br_{0.45}:Zn₂SnO₄ BHJ composite thin films possess enhanced and balanced charge carrier mobilities, superior film quality with enlarged crystal sizes, suppressed trap density, and reduced charge carrier extraction time. Photoluminescence and time-resolved photoluminescence studies demonstrated that there is an efficient photoinduced charge carrier transfer between CH₃NH₃PbI_{2,55}Br_{0,45} and Zn₂SnO₄ NPs. As a result, PSCs with BHJ device structures by the CH₃NH₃PbI_{2.55}Br_{0.45}:Zn₂SnO₄ thin film exhibited a V_{OC} of 1.10 V, a J_{SC} of 23.34 mA cm⁻², and an FF of 82.1%, with a corresponding PCE of 21.07%, all of which are higher than those (a J_{SC} of 22.23 mA cm⁻², a V_{OC} of 1.06 V, and an FF of 79.4%, with a corresponding PCE of 18.74%) of planar heterojunction PSCs by the pristine CH₃NH₃PbI_{2.55}Br_{0.45} thin film. In addition, BHJ PSCs by the

CH₃NH₃PbI_{2.55}Br_{0.45}:Zn₂SnO₄ thin film possess dramatically reduced photocurrent hysteresis, improved device stability, and reproducibility. All these results demonstrate that highperformance perovskite solar cells can be realized through bulk heterojunction device structures.

EXPERIMENTAL SECTION

Materials. Poly[bis(4-phenyl)(2,4,6-trimethyl phenyl)amine] (PTAA), lead iodide (PbI₂, 99.999%), methylammonium bromide (MABr), anhydrous DMF (99.8%), anhydrous ethanol (>99.5%), anhydrous toluene (99.8%), anhydrous chlorobenzene (CB, 99.8%), zinc chloride (ZnCl₂, 99.999%), and tin(IV) chloride pentahydrate (SnCl_a·5H₂O, 98%) were purchased from Sigma Aldrich and used as received without further purification. PC₆₁BM (99.5%) was purchased from Solenne BV and used as received without further purification. Methylammonium iodide (CH₃NH₃I (MAI)) was synthesized by using hydroiodic acid and methylamine in our laboratory. 5,15-1

Preparation and Characterization of Zn₂SnO₄ NPs. The solgel method was used to synthesis Zn₂SnO₄ NPs in our laboratory. The preparation procedures on Zn₂SnO₄ NPs are detailed in our previous publications.^{23,24} X-ray diffraction (XRD) performed on an X'Pert Pro was used to study the crystal structure and phase of Zn₂SnO₄ NPs. The film morphology and film microstructure were investigated by transmission electron microscopy (TEM) on a JEOL IEM-2100F. The preparation and characterization of Zn₂SnO₄ NPs are described in detail in Section S1.

Preparation of Perovskite Thin Films. PbI2 was added into the DMF solvent to make 400 mg mL⁻¹ PbI₂ DMF solution followed by stirring at 70 °C making cloudy solution to clear yellow solution. For the $CH_3NH_3PbI_{2.55}Br_{0.45}{:}Zn_2SnO_4$ thin film, PbI_2 DMF solution was first mixed with Zn₂SnO₄ NP DMF solution (tuning the volume ratio, making the weight percentages of Zn₂SnO₄:PbI₂ to be 5, 10, and 15%). A mixture of MAI-MABr (0.85:0.15 by molar ratio) was dissolved in the ethanol solvent to form 35 mg mL⁻¹ solution. The preparation procedures of CH3NH3PbI3 thin film are detailed in our previous publications. 5,15-17 The preparation procedures of the CH3NH3PbI3:Zn2SnO4 thin film are similar to that of the CH₃NH₃PbI₃ thin film, but using Zn₂SnO₄:PbI₂ as precursor solution rather than PbI₂ precursor solution.

Characterization of Perovskite Thin Films. Thin-film thickness was measured on a Dektak 150 surface profilometer. UV-vis absorption spectra of perovskite thin films were recorded on an HP 8453 spectrophotometer. Photoluminescence (PL) and time-resolved PL spectra of perovskite thin films were recorded on an FLS920 spectrofluorimeter (Edinburgh Instruments). Scanning electron microscope (SEM) images were obtained by using a field-emission scanning electron microscope (JEOL-7401). The grazing-incidence wide-angle X-ray scattering (GIWAXS) pattern was recorded on the dedicated high-resolution GIWAXS beamline (Sector 8-ID-E) in the Advanced Photon Source (APS), Argonne National Laboratory.⁵⁴ The space charge limited current method was used to estimate charge carrier mobilities of different perovskite films.

Fabrication and Characterization of Perovskite Solar Cells. The PTAA layer (~8 nm) was first deposited on precleaned ITOcoated glass substrates. The preparation method is detailed in our previous publication. Either pristine $CH_3NH_3PbI_{2.55}Br_{0.45}$ or CH₃NH₃PbI_{2.55}Br_{0.45}:Zn₂SnO₄ thin films were prepared by the twostep method described above. The thicknesses of $CH_3NH_3PbI_{2.55}Br_{0.45}$ and $CH_3NH_3PbI_{2.55}Br_{0.45}$: Zn_2SnO_4 thin films are measured to be ~340 and ~350 nm, respectively. Afterward, ~60 nm $PC_{61}BM$ was spin-coated on the top of the perovskite layer using $PC_{61}BM$ chlorobenzene solution (20 mg mL⁻¹). Lastly, a 100 nm Al was deposited on the top of the PC₆₁BM layer through a shadow mask in vacuum with a pressure of 4×10^{-6} mbar. The active device area was measured to be 0.045 cm².

The current density versus voltage (J-V) characteristics of PSCs were measured in the dark and under illumination by a solar simulator with a Keithly Model 2400 source measuring unit in our lab. The

detailed characterization of PSCs is described in the Supporting Information

ASSOCIATED CONTENT

Supporting Information

The Supporting Information is available free of charge on the ACS Publications website at DOI: 10.1021/acsami.9b12346.

Preparation and characterization of Zn₂SnO₄ NPs, device performance of perovskite solar cells, thin-film morphologies, absorption spectra, transient photocurrent measurement, electronic properties (PDF)

AUTHOR INFORMATION

Corresponding Author

*E-mail: xgong@uakron.edu. Fax: (330) 9723406.

ORCID ®

Xiong Gong: 0000-0001-6525-3824

Author Contributions

*W.X. and L.Z. contributed to this work equally.

The authors declare no competing financial interest.

ACKNOWLEDGMENTS

The authors thank the National Science Foundation (EECs 1351785 and EECs 1903303) and Air Force Office of Scientific Research (FA9550-15-1-0292) for financial support. The authors also thank Drs. Zhang Jiang and Joseph W. Strzalka at Argonne National Laboratory (DE-AC02-06CH11357).

REFERENCES

- (1) Grätzel, M. The Rise of Highly Efficient and Stable Perovskite Solar Cells. Acc. Chem. Res. 2017, 50, 487-491.
- (2) Jeon, N. J.; Na, H.; Jung, E. H.; Yang, T.-Y.; Lee, Y. G.; Kim, G.; Shin, H.-W.; Seok, S. I.; Lee, J.; Seo, J. A Fluorene-Terminated Hole-Transporting Material for Highly Efficient and Stable Perovskite Solar Cells. Nat. Energy 2018, 3, 682-689.
- (3) Seo, J.; Noh, J. H.; Seok, S. I. Rational Strategies for Efficient Perovskite Solar Cells. Acc. Chem. Res. 2016, 49, 562-572.
- (4) Jeon, N. J.; Noh, J. H.; Yang, W. S.; Kim, Y. C.; Ryu, S.; Seo, J.; Seok, S. I. Compositional Engineering of Perovskite Materials for High-Performance Solar Cells. Nature 2015, 517, 476-480.
- (5) Xu, W.; Zheng, L.; Zhang, X.; Cao, Y.; Meng, T.; Wu, D.; Liu, L.; Hu, W.; Gong, X. Efficient Perovskite Solar Cells Fabricated by Co Partially Substituted Hybrid Perovskite. Adv. Energy Mater. 2018, 8,
- (6) Son, D.-Y.; Lee, J.-W.; Choi, Y. J.; Jang, I.-H.; Lee, S.; Yoo, P. J.; Shin, H.; Ahn, N.; Choi, M.; Kim, D.; Park, N.-G. Self-formed grain boundary healing layer for highly efficient CH3NH3PbI3 Perovskite Solar Cells. Nat. Energy 2016, 1, 16081.
- (7) Tan, H.; Jain, A.; Voznyy, O.; Lan, X.; García de Arquer, F. P.; Fan, J. Z.; Quintero-Bermudez, R.; Yuan, M.; Zhang, B.; Zhao, Y.; Fan, F.; Li, P.; Quan, L. N.; Zhao, Y.; Lu, Z. H.; Yang, Z.; Hoogland, S.; Sargent, E. H. Efficient and Stable Solution-Processed Planar Perovskite Solar Cells via Contact Passivation. Science 2017, 355, 722-726.
- (8) Rong, Y.; Hu, Y.; Mei, A.; Tan, H.; Saidaminov, M.I.; Seok, S.I.; McGehee, M.D.; Sargent, E.H.; Han, H. Challenges for Commercializing Perovskite Solar Cells. Science 2018, 361, eaat8235.
- (9) Reid, O. G.; Yang, M.; Kopidakis, N.; Zhu, K.; Rumbles, G. Grain-Size-Limited Mobility in Methylammonium Lead Iodide Perovskite Thin Films. ACS Energy Lett. 2016, 1, 561-565.
- (10) Jung, H. S.; Park, N. G. Perovskite Solar Cells: from Materials to Devices. Small 2015, 11, 10-25.
- (11) Noel, N. K.; Abate, A.; Stranks, S. D.; Parrott, E. S.; Burlakov, V. M.; Goriely, A.; Snaith, H. J. Enhanced Photoluminescence and

- Solar Cell PerformanceviaLewis Base Passivation of Organic—Inorganic Lead Halide Perovskites. ACS Nano 2014, 8, 9815–9821.
- (12) McMeekin, D. P.; Sadoughi, G.; Rehman, W.; Eperon, G. E.; Saliba, M.; Hörantner, M. T.; Haghighirad, A.; Sakai, N.; Korte, L.; Rech, B.; Johnston, M. B.; Herz, L. M.; Snaith, H. J. A Mixed-Cation Lead Mixed-Halide Perovskite Absorber for Tandem Solar Cells. *Science* 2016, 351, 151–155.
- (13) Huang, X.; Wang, K.; Yi, C.; Meng, T.; Gong, X. Efficient Perovskite Hybrid Solar Cells by Highly Electrical Conductive PEDOT: PSS Hole Transport Layer. *Adv. Energy Mater.* **2016**, *6*, 1501773.
- (14) Edri, E.; Kirmayer, S.; Mukhopadhyay, S.; Gartsman, K.; Hodes, G.; Cahen, D. Elucidating the Charge Carrier Separation and Working Mechanism of CH₃NH₃PbI_{3-x}Cl_x Perovskite Solar Cells. *Nat. Commun.* **2014**, *5*, 3461.
- (15) Edri, E.; Kirmayer, S.; Henning, A.; Mukhopadhyay, S.; Gartsman, K.; Rosenwaks, Y.; Hodes, G.; Cahen, D. Why Lead Methylammonium Tri-Iodide Perovskite-Based Solar Cells Require a Mesoporous Electron Transporting Scaffold (but not Necessarily a Hole Conductor). *Nano Lett.* **2014**, *14*, 1000–1004.
- (16) Wang, K.; Liu, C.; Du, P.; Zheng, J.; Gong, X. Bulk Heterojunction Perovskite Hybrid Solar Cells with Large Fill Factor. *Energy Environ. Sci.* **2015**, *8*, 1245–1255.
- (17) Liu, C.; Wang, K.; Du, P.; Yi, C.; Meng, T.; Gong, X. Efficient Solution-Processed Bulk Heterojunction Perovskite Hybrid Solar Cells. *Adv. Energy Mater.* **2015**, *5*, 1402024.
- (18) Chiang, C.-H.; Wu, C.-G. Bulk Heterojunction Perovskite—PCBM Solar Cells with High Fill Factor. *Nat. Photonics* **2016**, *10*, 196–200.
- (19) Liu, Y.; Hong, Z.; Chen, Q.; Chang, W.; Zhou, H.; Song, T.-B.; Young, E.; Yang, Y.; You, J.; Li, G. Integrated Perovskite/Bulk-Heterojunction Toward Efficient Solar Cells. *Nano Lett.* **2015**, *15*, 662–668.
- (20) Kim, J.; Kim, G.; Back, H.; Kong, J.; Hwang, I.-W.; Kim, T. K.; Kwon, S.; Lee, J.-H.; Lee, J.; Yu, K.; Lee, C.-L.; Kang, H.; Lee, K. High-Performance Integrated Perovskite and Organic Solar Cells with Enhanced Fill Factors and Near-Infrared Harvesting. *Adv. Mater.* **2016**, *28*, 3159–3165.
- (21) Dong, S.; Liu, Y.; Hong, Z.; Yao, E.; Sun, P.; Meng, L.; Lin, Y.; Huang, J.; Li, G.; Yang, Y. Unraveling the High Open Circuit Voltage and High Performance of Integrated Perovskite/Organic Bulk-Heterojunction Solar Cells. *Nano Lett.* **2017**, *17*, 5140–5147.
- (22) Singh, R.; Shukla, V. K. ITIC-Based Bulk Heterojunction Perovskite Film Boosting the Power Conversion Efficiency and Stability of the Perovskite Solar Cell. Sol. Energy 2019, 178, 90–97.
- (23) Zheng, X.; Troughton, J.; Gasparini, N.; Lin, Y.; Wei, M.; Hou, Y.; Liu, J.; Song, K.; Chen, Z.; Yang, C.; et al. Quantum Dots Supply Bulk- and Surface-Passivation Agents for Efficient and Stable Perovskite Solar Cells. *Joule* 2019, 1963.
- (24) de Haas, M. P.; Warman, J. M.; Anthopoulos, T. D.; de Leeuw, D. M. The Mobility and Decay Kinetics of Charge Carriers in Pulse-Ionized Microcrystalline PCBM Powder. *Adv. Funct. Mater.* **2006**, *16*, 2274–2280.
- (25) Shin, S. S.; Yang, W. S.; Noh, J. H.; Suk, J. H.; Jeon, N. J.; Park, J. H.; Kim, J. S.; Seong, W. M.; Seok, S. I. High-Performance Flexible Perovskite Solar Cells Exploiting Zn₂SnO₄ Prepared in Solution Below 100 C. *Nat. Commun.* **2015**, *6*, 7410.
- (26) Huang, X.-J.; Yao, X.; Xu, W.-Z.; Wang, K.; Huang, F.; Gong, X.; Cao, Y. Inverted Polymer Solar Cells with Zn₂SnO₄ Nanoparticles as the Electron Extraction Layer. *Chin. Chem. Lett.* **2017**, 28, 1755–1759.
- (27) Yang, M.; Zhang, T.; Schulz, P.; Li, Z.; Li, G.; Kim, D. H.; Guo, N.; Berry, J. J.; Zhu, K.; Zhao, Y. Facile Fabrication of Large-Grain CH₃NH₃PbI_{3-x}Br_x Films for High-Efficiency Solar Cells via CH₃NH₃Br-Selective Ostwald Ripening. *Nat. Commun.* **2016**, *7*, 12305.
- (28) Gao, P.; Grätzel, M.; Nazeeruddin, M. K. Organohalide Lead Perovskites for Photovoltaic Applications. *Energy Environ. Sci.* **2014**, *7*, 2448–2463.

- (29) Kim, D. W.; Shin, S. S.; Cho, I. S.; Lee, S.; Kim, D. H.; Lee, C. W.; Jung, H. S.; Hong, K. S. Synthesis and Photovoltaic Property of Fine and Uniform Zn₂SnO₄ nanoparticles. *Nanoscale* **2012**, *4*, 557–562.
- (30) Alpuche-Aviles, M. A.; Wu, Y. Photoelectrochemical Study of the Band Structure of Zn₂SnO₄ Prepared by the Hydrothermal Method. *J. Am. Chem. Soc.* **2009**, *131*, 3216–3224.
- (31) Wang, J. X.; Xie, S. S.; Yuan, H. J.; Yan, X. Q.; Liu, D. F.; Gao, Y.; Zhou, Z. P.; Song, L.; Liu, L. F.; Zhao, X. W.; Dou, X. Y.; Zhou, W. Y.; Wang, G. Synthesis, Structure, and Photoluminescence of Zn₂SnO₄ Single-Crystal Nanobelts and Nanorings. *Solid State Commun.* **2004**, *131*, 435–440.
- (32) Venkatesan, N. R.; Labram, J. G.; Chabinyc, M. L. Charge-Carrier Dynamics and Crystalline Texture of Layered Ruddlesden—Popper Hybrid Lead Iodide Perovskite Thin Films. *ACS Energy Lett.* **2018**, *3*, 380–386.
- (33) Seifter, J.; Sun, Y.; Heeger, A. J. Transient Photocurrent Response of Small-Molecule Bulk Heterojunction Solar Cells. *Adv. Mater.* **2014**, *26*, 2486–2493.
- (34) Cowan, S. R.; Street, R. A.; Cho, S.; Heeger, A. J. Transient Photoconductivity in Polymer Bulk Heterojunction Solar Cells: Competition between Sweep-Out and Recombination. *Phys. Rev. B* **2011**, 83, No. 035205.
- (35) Shao, Y.; Xiao, Z.; Bi, C.; Yuan, Y.; Huang, J. Origin and Elimination of Photocurrent Hysteresis by Fullerene Passivation in CH₃NH₃PbI₃ Planar Heterojunction Solar Cells. *Nat. Commun.* **2014**, *5*, 5784.
- (36) Seifter, J.; Sun, Y.; Choi, H.; Lee, B. H.; Nguyen, T. L.; Woo, H. Y.; Heeger, A. J. Measurement of the Charge Carrier Mobility Distribution in Bulk Heterojunction Solar Cells. *Adv. Mater.* **2015**, *27*, 4989–4996.
- (37) Bube, R. H. Trap Density Determination by Space-Charge-Limited Currents. *J. Appl. Phys.* **1962**, 33, 1733–1737.
- (38) Shi, D.; Adinolfi, V.; Comin, R.; Yuan, M.; Alarousu, E.; Buin, A.; Chen, Y.; Hoogland, S.; Rothenberger, A.; Katsiev, K.; Losovyj, Y.; Zhang, X.; Dowben, P. A.; Mohammed, O. F.; Sargent, E. H.; Bakr, O. M. Low Trap-State Density and Long Carrier Diffusion in Organolead Trihalide Perovskite Single Crystals. *Science* 2015, 347, 519–522.
- (39) Riedel, I.; Parisi, J.; Dyakonov, V.; Lutsen, L.; Vanderzande, D.; Hummelen, J. C. Effect of Temperature and Illumination on the Electrical Characteristics of Polymer-Fullerene Bulk-Heterojunction Solar Cells. *Adv. Funct. Mater.* **2004**, *14*, 38–44.
- (40) Azmi, R.; Oh, S.-H.; Jang, S.-Y. High-Efficiency Colloidal Quantum Dot Photovoltaic Devices Using Chemically Modified Heterojunctions. *ACS Energy Lett.* **2016**, *1*, 100–106.
- (41) Mihailetchi, V. D.; Xie, H. X.; de Boer, B.; Koster, L. J. A.; Blom, P. W. M. Charge Transport and Photocurrent Generation in Poly (3-Hexylthiophene): Methanofullerene Bulk-Heterojunction Solar Cells. *Adv. Funct. Mater.* **2006**, *16*, 699–708.
- (42) Fabregat-Santiago, F.; Garcia-Belmonte, G.; Mora-Seró, I.; Bisquert, J. Characterization of Nanostructured Hybrid and Organic Solar Cells by Impedance Spectroscopy. *Phys. Chem. Chem. Phys.* **2011**, *13*, 9083–9118.
- (43) Gonzalez-Pedro, V.; Juarez-Perez, E. J.; Arsyad, W.-S.; Barea, E. M.; Fabregat-Santiago, F.; Mora-Sero, I.; Bisquert, J. General Working Principles of CH₃NH₃PbX₃ Perovskite Solar Cells. *Nano Lett.* **2014**, *14*, 888–893.
- (44) Wetzelaer, G.-J. A. H.; Scheepers, M.; Sempere, A. M.; Momblona, C.; Ávila, J.; Bolink, H. J. Trap-Assisted Non-Radiative Recombination in Organic-Inorganic Perovskite Solar Cells. *Adv. Mater.* **2015**, *27*, 1837–1841.
- (45) Sze, S. M.; Ng, K. K. Physics of Semiconductor Devices; John Wiley & Sons, 2006.
- (46) Laban, W. A.; Etgar, L. Depleted Hole Conductor-Free Lead Halide Iodide Heterojunction Solar Cells. *Energy Environ. Sci.* **2013**, *6*, 3249–3253.
- (47) Liu, Y.; Renna, L. A.; Page, Z. A.; Thompson, H. B.; Kim, P. Y.; Barnes, M. D.; Emrick, T.; Venkataraman, D.; Russell, T. P. A

- Polymer Hole Extraction Layer for Inverted Perovskite Solar Cells from Aqueous Solutions. *Adv. Energy Mater.* **2016**, *6*, 1600664.
- (48) Cai, F.; Cai, J.; Yang, L.; Li, W.; Gurney, R. S.; Yi, H.; Iraqi, A.; Liu, D.; Wang, T. Molecular Engineering of Conjugated Polymers for Efficient Hole Transport and Defect Passivation in Perovskite Solar Cells. *Nano Energy* **2018**, *45*, 28–36.
- (49) Kim, H.-S.; Park, N.-G. Parameters AffectingI–V Hysteresis of CH₃NH₃PbI₃ Perovskite Solar Cells: Effects of Perovskite Crystal Size and Mesoporous TiO₂ Layer. *J. Phys. Chem. Lett.* **2014**, *5*, 2927–2934.
- (50) Zhao, C.; Chen, B.; Qiao, X.; Luan, L.; Lu, K.; Hu, B. Revealing Underlying Processes Involved in Light Soaking Effects and Hysteresis Phenomena in Perovskite Solar Cells. *Adv. Energy Mater.* **2015**, *5*, 1500279.
- (51) Meloni, S.; Moehl, T.; Tress, W.; Franckevičius, M.; Saliba, M.; Lee, Y.H.; Gao, P.; Nazeeruddin, M.K.; Zakeeruddin, S.M.; Rothlisberger, U.; Graetzel, M. Ionic Polarization-Induced Current—Voltage Hysteresis in CH₃NH₃PbX₃ Perovskite Solar Cells. *Nat. Commun.* **2016**, *7*, 10334.
- (52) Niu, G.; Guo, X.; Wang, L. Review of Recent Progress in Chemical Stability of Perovskite Solar Cells. *J. Mater. Chem. A* **2015**, 3, 8970–8980.
- (53) Xiao, Z.; Dong, Q.; Bi, C.; Shao, Y.; Yuan, Y.; Huang, J. Solvent Annealing of Perovskite-Induced Crystal Growth for Photovoltaic-Device Efficiency Enhancement. *Adv. Mater.* **2014**, *26*, 6503–6509.
- (54) Wang, K.; Zheng, L.; Zhu, T.; Yao, X.; Yi, C.; Zhang, X.; Cao, Y.; Liu, L.; Hu, W.; Gong, X. Efficient Perovskite Solar Cells by Hybrid Perovskites Incorporated with Heterovalent Neodymium Cations. *Nano Energy* **2019**, *61*, 352–360.